



UNIVERSITÀ  
DI TRENTO

Dipartimento di  
Fisica



# NANOSCIENCE LABORATORY HIGHLIGHTS 2021

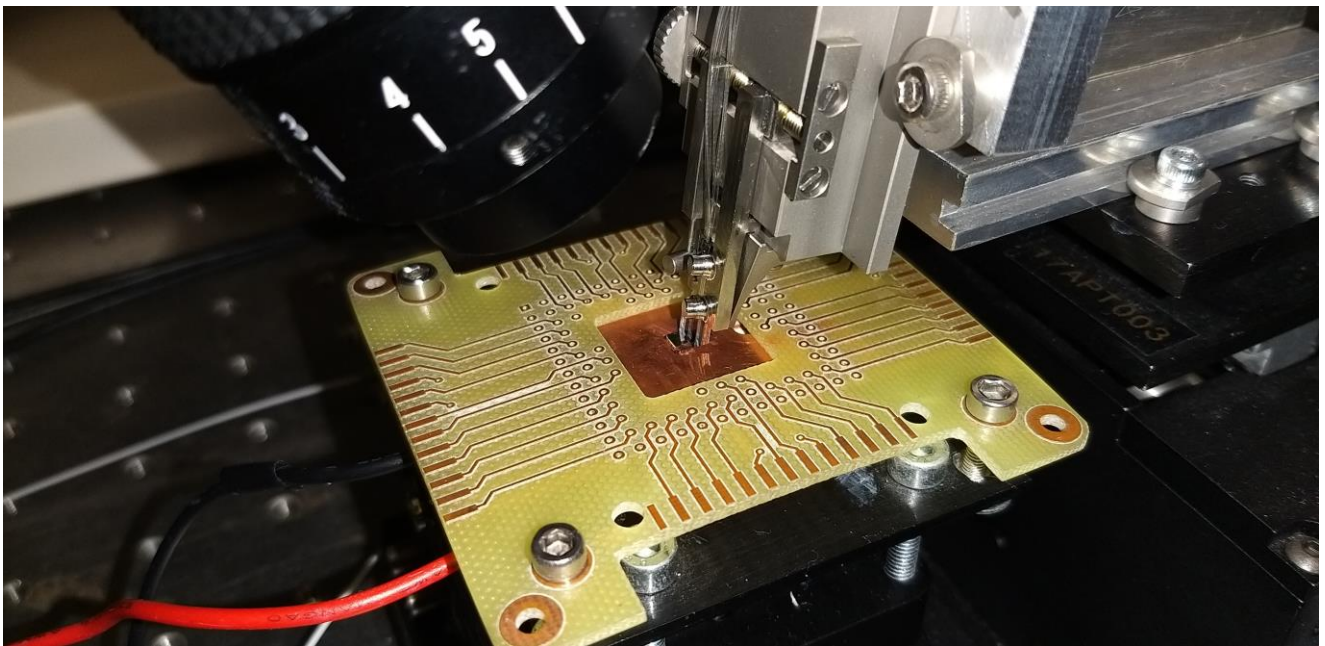


*Image on the front cover: a photograph of a photonic chip under test on a PPCB board (courtesy of Lorenzo Pavesi)*

## NANOSCIENCE LABORATORY

### MEMBERS (2021)

#### Faculty staff

Lorenzo Pavesi (full professor, head)  
 Marina Scarpa (full professor)  
 Zeno Gaburro (associate professor)  
 Paolo Bettotti (associate professor)  
 Stefano Azzini (assistant professor)  
 Mattia Mancinelli (researcher)  
 Beatrice Vignoli (researcher)

#### Technical staff

Enrico Moser  
 Elvira D'Amato

#### Post-docs

Stefano Signorini (left November 2021)  
 Stefano Biasi  
 Massimo Borghi (left October 2021)  
 Ilya Auslender  
 Hum Nath Parajuli

#### Administrative staff

Chiara Rindone

#### Doctoral students

Chiara Vecchi (left April 2021)  
 Clara Zaccaria  
 Davide Bazzanella  
 Nicolò Leone  
 Riccardo Franchi  
 Giovanni Donati  
 Matteo Sanna  
 Johanna Mae Indias (left November 2021)  
 Yasaman Heydari

#### Master students

Filippo Mione  
 Marco Peretti  
 Davide Rizzotti  
 Emiliano Staffoli  
 Lorenzo Cerini

### SCIENTIFIC MISSION

#### Introduction to the Nanoscience Laboratory

The Nanoscience Laboratory (NL) is one of the scientific groups of the Department of Physics, University of Trento. Its main areas of research are neuromorphic photonics, integrated quantum photonics, linear and nonlinear silicon photonics, non-Hermitian photonics and nanobiotechnologies. The mission of NL is to generate new knowledge, to develop understanding and to spin-off applications from physical phenomena associated with photons and their interactions with matter, particularly when it is nanostructured. Specifically, NL aims at understanding the optical properties of lightwave systems such as optical waveguides, microresonators and complex dielectric systems. NL covers the whole value chain from fundamental phenomena to device applications, where the photonic platform is compatible with the main driving silicon microelectronic technologies. However, silicon is not the only material studied. Other fields of interest concern the use of cellulose to tailor the properties of nanostructure atom-by-atom or the use of biological neurons to study memory formation.

NL research group consists of more than 25 people with different scientific backgrounds. Researchers from physics, physiology, bio-chemistry, materials science and electrical engineering are gathered to form a group of interdisciplinary nature. It is worth mentioning that NL collaborates

closely with the Sensors and Devices research center of the Fondazione Bruno Kessler (FBK). This collaboration spans over the last thirty years and covers various themes such as fabrication, testing and application of biomaterials and silicon based devices. Both participate in many common projects. The current ones are: projects EPIQUS, LESSO, QRANGE and Q@TN. A further strategic collaboration is ongoing with the Trento units of CNR-INO, specifically dedicated to implement quantum optics in integrated silicon chip.

Moreover, with the support of FBK and CNR and every odd year, NL organizes a winter school on optoelectronics and photonics. The 11<sup>th</sup> edition was on “Neuromorphic Photonics” on 20-26 June 2021 in Monte Bondone. Furthermore, the members of NL are often invited to participate in the organizing committees of international conferences or workshops.

The research activities of NL are mainly supported by the local government (PAT), by the European Commission, by the Italian Ministry of University and Research (MUR) and by companies. During the period covered by these Highlights, NL has been and is involved in the following projects: PRIN PELM “Photonics Extreme Learning Machine: from neuromorphic computing to universal optical interpolant, strain gauge sensor and cancer morphodynamic monitor”; PRIN PANACEA “A technology PIatform for the sustainable recovery and advanced use of NANOstructured CELLulose from Agri-food residues”; ERC-2017-ADG-788793 BACKUP:

“Unveiling the relationship between brain connectivity and function by integrated photonics”; ERC-2020-POC-963463 ALPI: “All optical signal recovery by Photonic neural network Integrated in a transceiver module”; H2020-FETFLAG-2018-03 QRANGE: “Quantum Random Number Generators: cheaper, faster and more secure”; Q@TN joint lab “Quantum Science and Technology in Trento”; India-Trento Program for Advanced Research - ITPAR: “A cheap, light, compact source for QKD based on intraparticle entanglement in an integrated photonic circuit”; ASI - LESSO: “Laser etero-integrato a stato solido per trappole ottiche”; NANOFARM (Legge Provinciale 13 dicembre, 1999 n. 6); H2020-MSCA-IF-2020- 101033260 ISLAND: “An integrated setup for in-vitro optogenetic experiments using AI to localize stimulation with a feedback of electrophysiological signals”.

### Silicon Nanophotonics

Silicon photonics is the technology where photonic devices are produced by standard microelectronic processes using the same paradigm of electronics: integration of a large number of devices to yield a high circuit complexity, which allows for high performances and low costs. Here, the truth is to develop photonic devices that can be easily integrated to improve the single device performance and to allow high volume production.

We are following three different research directions: Quantum Photonics, Neuromorphic Photonics and non-Hermitian Photonics. On one side, we will develop new scheme to implement artificial intelligent in a photonic silicon chip by using brain-inspired or neuromorphic computing schemes. On the other side, we will use silicon photonics to provide a suitable platform for quantum computing and quantum simulations. And finally, we will use the intrinsic dissipative propagation of light to study non-Hermitian systems. In all these approaches, one fundamental device is the silicon microresonator where whispering gallery modes exist. Their nonlinearities can be used to generate new quantum states of light or to realize recurrent neural network. In addition, new physics can be studied with micro-disks or micro-rings, e.g. chirality, exceptional points, frequency comb generation, entangled photon generation. Also, multimode waveguides are used for nonlinear frequency conversion or generation.

To develop silicon photonics, one further add-on is making silicon to do something that it is not able to do in its standard (bulk) form. Low dimensional silicon, where small silicon nanocrystals or nanoclusters (Si-nc) are developed, is one way to compel silicon to act as an active optical material. Alternatively, we use the built-in or p-i-n induced electric fields to tune the non-linear optical properties of silicon waveguides for the development of new MIR sources (parametric generation via second order effects or frequency comb generation). Nonlinear optics is finally used to gen-

erate pairs of entangled photons, which in turn feed quantum interferometers or integrated quantum photonic circuits.

Lastly, hybrid chips are developed to interface living neurons with photonic waveguides in the search for artificial intelligence. Here, the signal transduction is achieved by using photo-sensitive proteins.

### Advanced nanomaterials for energy, environment and life

In this research activity, we learn from nature how to use molecules or biological nanostructures to build materials with specific features. The focus is on understanding the properties of colloids of biological origin, the dynamics at the bio-interfaces, the strength and stability of natural structures. The final goal is to transfer the acquired knowledge on innovation by developing sustainable and smart materials and processes.

### Experimental facilities

The NL facilities allow for detailed experimental studies in nanoscience, photonics and biotechnologies. Since the effective collaboration with FBK most material processing and device productions are performed within their premises. For photonics, we have facilities to cover the light spectrum from the THz to UV ranges with whatever time resolution is needed. Laser sources comprehends: Ti-sapphire fs-ps laser (1 W average over 1000-700 nm, 2 ps or 70 fs pulses, 82 MHz repetition rate) interfaced with a second harmonic generator and pulse picker; TOPAS pumped with an amplified Ti:Sa laser which covers the 1-2.6  $\mu\text{m}$  range with 35 fs, 10 kHz, 3 mJ; 2W tunable CW Cr:ZnSe/S fiber-bulk hybrid laser to cover the 2-3  $\mu\text{m}$  range; four tunable CW lasers (850-870 nm, 1200 - 1700 nm and 1500 - 1600nm) fiber pig-tailed; high power fiber-laser at 1550 nm (1-100 MHz, 50 ps); 4W EDFA and 2W semiconductors amplifiers, a supercontinuum light source (410-2400 nm, 1W), several pig-tailed diode lasers, ASE source at 1550 nm and a broad band SLD at 800 nm; three high-power true-CW DPSS single-line laser operating at 532, 473 and 355 nm. Detectors comprehend: visible and infrared photomultipliers and CCDs, a visible streak camera with ps resolution, 4K cooled bolometers which cover THz region, avalanche photodiodes for vis and IR ranges plus many single photon detectors in the visible and IR. Two home-made MIR single photon-counters. To perform spectral analysis several set-ups are available: FTIR and dispersive spectrophotometers, a micro-Raman setup, a micro-FTIR and a UV-vis-IR spectrophotometer (shared with other laboratories), UV-Vis and fluorescence spectrophotometer dedicated to biochemical experiments. Eight set-ups are dedicated to the characterization of waveguides equipped with nanopositioning systems and polarization controllers, each specified on a given function: visible, visible broad range, quantum, passive infrared, high speed infrared, non-linear infrared, non-linear MIR and on wafer. A set-up is dedicated to high

speed measurements, with 80 Gbps capability where a 60 GHz arbitrary waveform generator, electro-optical modulators, coherent detectors and a four channels, 20 GHz oscilloscope. Other devices are: - a solar simulator for cells up to 5 inches in size; - two nanoprobe stations (AFM and SNOM) - two semiconductor probe stations (4 and 8 inches) and different electrical characterization systems (I-V, Z- $\Omega$ , EL-I, etc.). Four VIS to NIR optical spectrum analyzers are available. A probe station is interfaced by a fibres bundle with a spectrometer equipped with nitrogen cooled visible and IR CCDs. An electrochemical laboratory with various chemical hoods, galvanostats and volt-ameters is available for sample processing. For optical, electrical and molecular dynamics simulations, the laboratory uses free and commercial software and has a work-station with 4 GPU. Two laboratories are also available, one dedicated to chemical synthesis and the other to the preparation of biological samples. Two other laboratories with biological hoods, incubators and confocal microscopes are dedicated to biological experiments. In one, a confocal microscope with an insert for electrophysiology (MEA) and optogenetics measurement equipped with a "spinning disk" system for fast acquisitions and a super-resolution system.

#### 2021 Publications

- D. Bazzanella, G. Bincoletto, M. Consolandi, M. Fasan, F. Gennari, F. C. La Vattiata, L. Rinaldi, D. Roccaro, C. Zaccaria, "Artificial and Biological Neurons: Interdisciplinary Issues and Future Perspectives", *BioLaw Journal – Rivista di Bio-Diritto* n. 1/2021, pp. 353-379 (2021)
- M. Borghi, D. Bazzanella, M. Mancinelli and L. Pavesi "On the modeling of thermal and free carrier nonlinearities in Silicon On Insulator microring resonators", *Optics Express* 29, 4363-4377 (2021)
- C. Zaccaria, M. Mancinelli, L. Pavesi, "A FEM enhanced Transfer Matrix method for optical grating design" *Journal of Lightwave Technology* 39, 3521 (2021)
- A. Muñoz de las Heras, R. Franchi, S. Biasi, M. Ghulinyan, L. Pavesi, and I. Carusotto, "Nonlinearity-Induced Reciprocity Breaking in a Single Nonmagnetic Taiji Resonator", *Phys. Rev. Applied* 15, 054044 (2021)
- M. Borghi, S. Biasi, L. Pavesi, "Reservoir computing based on a silicon microring and time multiplexing for binary and analog operations", *Scientific Reports* 11, 15642 (2021)
- S. Mazzucchi, N. Leone, S. Azzini, L. Pavesi, V. Moretti, "Entropy certification of a realistic quantum random-number generator based on single-particle entanglement", *Phys. Rev. A* 104, 022416 (2021)
- R. Franchi, S. Biasi, A. Muñoz de las Heras, M. Ghulinyan, I. Carusotto and L. Pavesi, "Influence of the bus waveguide on the linear and nonlinear response of a taiji microresonator", *Optics Express* 29, 29615 (2021)
- Runkui Yao, Hongxiang Li, Bohao Zhang, Weiwei Chen, Pengjun Wang, Shixun Dai, Yuxiao Liu, Jun Li, Yan Li, Qiang Fu, Tingge Dai, Hui Yu, Jianyi Yang, Lorenzo Pavesi, "Compact and Low-Insertion-Loss  $1 \times N$  Power Splitter in Silicon Photonics" *Journal of Lightwave Technology* 39, 6253 (2021)
- L. Minati, M. Mancinelli, M. Frasca, P. Bettotti and L. Pavesi, "An analog electronic emulator of non-linear dynamics in optical microring resonators", *Chaos, Solitons and Fractals* 153, 111410 (2021)
- B. Vignoli, G. Sansevero, M. Sasi, R. Rimondini, R. Blum, V. Bonaldo, E. Biasini, S. Santi, N. Berardi, B. Lu, M. Canossa, "Astrocytic microdomains from mouse cortex gain molecular control over long-term information storage and memory retention", *Commun Biol* 4, 1152 (2021)
- Lorenzo Pavesi, "Thirty Years in Silicon Photonics: A Personal View", *Frontiers in Physics* 9, 786028 (2021)
- S. Signorini, M. Sanna, S. Piccione, M. Ghulinyan, P. Tide- mand-Lichtenberg, C. Pedersen and L. Pavesi, "A silicon source of heralded single photons at  $2 \mu\text{m}$ ", *APL Photonics* 6, 126103 (2021)
- P. Bettotti, M. Scarpa, "Nanocellulose and its interface: on the road to the design of emerging materials", *Adv. Materials Interfaces* 9, 2101593 (2022)
- N. Ferrari, CA Maestri, P. Bettotti, M. Grassi, M. Abrami, M. Scarpa, "Effect of Process Conditions and Colloidal Properties of Cellulose Nanocrystals Suspensions on the Production of Hydrogel Beads", *Molecules* 26, 2552 (2021)

- P. Lecca, M. Lecca, CA Maestri, M. Scarpa, M. “Biexponential fitting for noisy data with error propagation” Math Meth App Sci. 44, 10154 (2021)

#### 2021 Patents

- MODULO OTTICO DI TRASMISSIONE-RICEZIONE CON RETE NEURALE (Inventori: Mancinelli Mattia, Bettotti Paolo, Pavesi Lorenzo. IT domanda 102021000011357 del 4 Maggio 2021)

#### 2021 PhD Thesis

- Chiara Vecchi “Second harmonic generation in engineered silicon waveguides” (7 April 2021)

#### 2021 Books

- Silicon Photonics IV: Innovative Frontiers, David J. Lockwood, Lorenzo Pavesi editors, Topics in Applied Physics, Springer vol 139 (Springer Verlag, Berlin 2021)

#### Project web sites

<http://nanolab.physics.unitn.it/>

<https://r1.unitn.it/back-up/>

<https://r1.unitn.it/back-up/erc-poc-alpi-project/>

<https://epiquis.fbk.eu/>

<https://grange.eu/>

<https://sites.google.com/unitn.it/panacea/home>

<https://r1.unitn.it/pelm/>

<https://r1.unitn.it/back-up/projects/projects/island-project/>

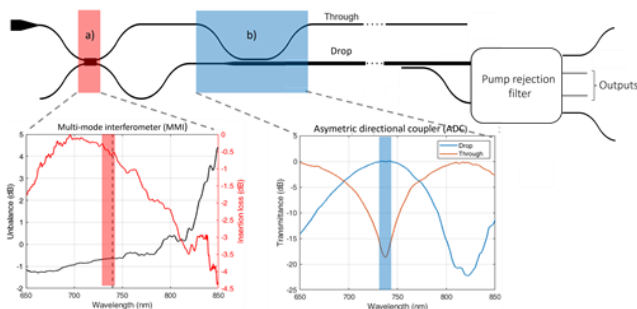
<https://www.quantumtrento.eu/>

## 1. Integrated photonic devices for a quantum simulator in Silicon-Oxynitride (Matteo Sanna, Massimo Borghi, Stefano Azzini)

Quantum simulators are controllable quantum systems that can be used to imitate large-scale quantum problems of interest in biology, chemistry and solid-state physics. They allow tackling problems that are intractable to conventional classical computers. Several physical systems can be used to realize quantum simulators; one of these is integrated quantum photonics. Here, photons can be easily manipulated and individually addressed with high precision using optical components operating at room temperature, without the need for cryogenic systems. The behavior of photons allow the simulation of complex and non-local many-body interactions.

We are developing a Silicon-Oxynitride photonic platform in the near-infrared (NIR) spectral region, where silicon single-photon avalanche diode (SPAD) detectors will be monolithically integrated to realize a photonic quantum simulator (QS) device, in the framework of the European project EPIQUS (Electronic-Photonic integrated quantum simulator platform). Here, the photon source is based on intermodal Spontaneous Four-Wave Mixing (SFWM). Through this spontaneous process, using a pulsed laser at 740 nm, we can generate two photons, which are energy-time correlated. By exploiting the intermodal properties, we will generate twin photons in discrete bands spectrally distant from the pump photons. This will facilitate the removal of the residual pump, to finally give photons pairs in input at the quantum simulator.

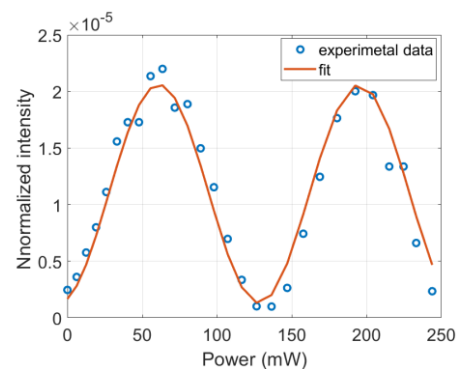
As a first step in the development of a dedicated photonic platform, we designed and characterized the fundamental building blocks used to assemble both the source and the unitary matrices for quantum simulation. Fig. 1 shows the scheme for the generation of entangled photons.



**Figure 1:** Sketch of the photon pair source. In a) we show the main metrics of the 2x2 splitter as a function of wavelength. These are the insertion loss (red line) and the unbalance (black line) between the output ports. In b) the ADC is shown. In the figure below on the right, the blue line describes the output of the coupled waveguide and the orange line the residual beam on the starting waveguide as the wavelength changes. The two highlighted bars in the graphs show the wavelength of 740 nm

Integrated 2x2 beam-splitters (Fig. 1a) based on multimode interference are used to both split the pump into several coherent channels and to realize the Mach Zehnder interferometers (MZI). The latter lays at the basis of the realization of pump rejection filters, and will constitute the elementary block from which unitary transformations on the spatial modes of the signal and idler photon will be constructed. At the current stage, the 50/50 splitter has a residual unbalance between its outputs of less than 0.6 dB at 740 nm (black curve). Here, it is observed that the insertion loss (red curve) is less than 0.5 dB. In Fig. 1b we show the performance of Asymmetric Directional Couplers, which are used both to prepare the pump in a coherent superposition of a TE0 mode and a TE1 mode (to exploit the intermodal SFWM), and to separate the pair of co-propagating photons. The latter allows getting both beams on the TE0 mode of two separate waveguides.

The figure shows the blue line corresponding to the dropped beam in the coupled waveguide and the orange line describing the residual intensity remaining in the first waveguide. It is observed that, at 740 nm, a good drop in the coupled waveguide (blue line) and a correspondingly low residual beam (orange line) in the continuing waveguide are obtained.



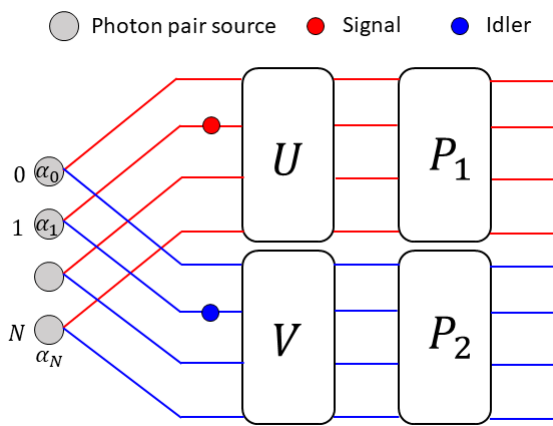
**Figure 2:** The phase-power relationship of an MZI at 740 nm is shown. The blue circles are the experimental measurements, while the orange curve is a fit

Figure 2 shows how the thermo-optic effect of the material affects the transmitted intensity of a MZI. Air trenches have been realized on both sides of the waveguides on top of which a heater is placed at a suitable distance. In order to obtain a phase variation of  $\pi$  of the MZI transfer function 79 mW of electrical power must be supplied. The use of air trenches allows for greater thermal isolation of heated waveguides, resulting in a lower electrical power loss. The next step is the characterization of the SFWM sources, underway at the time of writing.

## 2. Implementation of a variational quantum eigensolver on a silicon chip (Alessio Baldazzi, Massimo Borghi)

Quantum computing promises an exponential speedup over classical machines for certain problems; however, the

hardware demands consign this aim to the longer term. Today's quantum processors are limited in terms of qubit number, interconnection topology, and fidelity of the entangling gates. They are prone to loss, reason why they are termed as Noise Intermediate Scale Quantum (NISQ) devices. In this work, we experimentally implement variational quantum algorithms including the Variational Quantum Eigensolver (VQE) and the Quantum Approximate Optimisation Algorithm (QAOA) on integrated photonic devices. These are leading candidates for realizing a useful quantum advantage on NISQ processors, since they require a modest number of qubits, a limited circuit depth and can produce accurate results without error correction. We implement a qubit-photon encoding which utilizes the bipartite, high-dimensional entanglement between two photons produced by sources of two-mode squeezed vacuum.



**Figure 3:** High-level layout of the state preparation and measurement for the VQE and QAOA. Unitaries are implemented through a network of programmable phase shifters and splitters. Sources of photon pairs are based on Spontaneous Four Wave Mixing in Silicon waveguides.

As shown in Fig. 3,  $N=2^C$  photon pair sources are coherently pumped with amplitudes  $\alpha_1, \dots, \alpha_N$ . By post-selecting only those outcomes where two photons are detected, the entangled state  $|\Psi\rangle = \sum \alpha_k |k\rangle_s |k\rangle_i$  is generated after the sources, where  $k=\{1, \dots, N\}$  labels the spatial mode of the photon. The dimension of the Hilbert space is  $N^2 = 2^{2C}$ , which is equivalent to the one of  $2C$  qubits. Two unitaries  $U$  and  $V$  are then applied to the two parties, each carrying  $C$  qubits of information. The form of  $U$  and  $V$  is tailored from the Schmidt decomposition of the bipartite state to prepare arbitrary  $C$ -qubit states. This is used to generate the parametrized ansatz states for the VQE or the QAOA, which are then measured using the set of Positive Operator Valued Measure (POVM)  $P_1$  and  $P_2$ . This final step evaluates the cost function to be optimized. In the case of quantum chemistry, the latter is typically the expectation value of some electronic Hamiltonian. For

generic optimization problems, such as the ones carried on a complex connected graph, an equivalent Hamiltonian formulation is synthesized first, and then QAOA is run to minimize the energy. We use a large scale photonic chips of the works to simulate systems up to 8 qubits for pure states and 4 qubits for mixed states. All the building blocks described so far are programmable through thermo-optic phase shifters, and fit within a chip size of few  $\text{cm}^2$ . Using 4 qubits, we experimentally demonstrated the use of VQE to find the ground state energy and the electronic configuration of the Hydrogen molecule, and successfully implemented QAOA to solve combinatorial graph problems (MaxCut and Minimum Vertex Cover). Figure 4 shows an example of the energy of the Hydrogen molecule as a function of the variational parameter  $\theta$ , which controls the amount of contribution of the anti-bonding orbital to the equilibrium configuration. We are now running experiments on larger molecular systems, such as  $\text{H}_2\text{O}$  and  $\text{He}$ , and using QAOA to solve graph search problems up to 8 vertices.

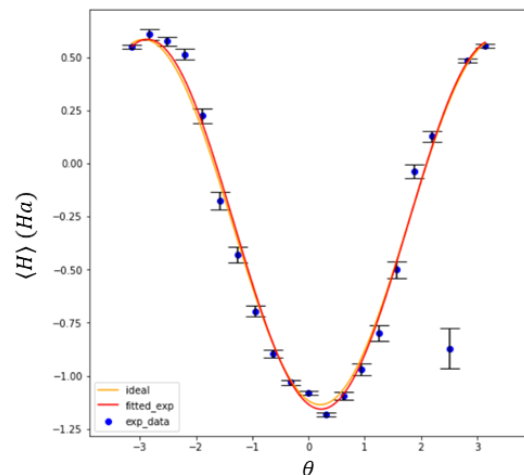


**Figure 4:** Expectation value of the electronic Hamiltonian of Hydrogen as a function of the single variational parameter  $\theta$ . The ground state energy has a dominant contribution ( $\propto \cos(\theta)$ ) coming from two molecular bonding orbitals with opposite spins, and a small contribution ( $\propto \sin(\theta)$ ) arising from anti-bonding orbitals. The minimum is found at  $\theta \sim 0.22$  and corresponds to an energy of  $-1.136 \text{ Ha}$ .

This work is done in collaboration with the Quantum Engineering and Technology labs, University of Bristol. We acknowledge Mr. David Robers, Dr. Alex Jones and prof. Anthony Laing.

### 3. Spectrally tunable photon pairs by Intermodal Four Wave Mixing for large arrays of indistinguishable sources (Massimo Borghi)

Large-scale silicon photonics quantum processors require photon pair sources with outstanding metrics in terms of

indistinguishability and purity of the heralded single photon states. Delayed-pump Intermodal Four Wave Mixing (IFWM) in multimode waveguides has been recently proven to simultaneously fulfil these metrics. In this scheme, pair emission occurs in narrow spectral bands (few nm) largely detuned with respect to the pump beam. This is achieved by engineering the phase matching relation through the waveguide cross-section and the choice of the transverse modes involved in the process. Matching the emission bandwidth to the one of the pump strongly reduces the frequency anti-correlation of the photon pairs, yet is not sufficient to reach heralded single photon purities above 99%. The residual correlations comes from the abrupt turn on of the IFWM process, which occurs when the pump beam enters the nonlinear waveguide. To erase this information, the two pump pulses are coupled in different modes, and the fastest is slightly delayed with respect to the other. In this way, an adiabatic switching of the nonlinear interaction occurs within the waveguide as the two pulses gradually overlap. This scheme allowed reaching a spectral purity of 99.04%, and a record Heralded Hong Ou Mandel (HHOM) visibility of 96% between photons heralded from independent sources. Despite this, the scheme still lacks of the spectral tunability, which would allow coping with the unavoidable presence of fabrication inhomogeneities. By tapering the width of the waveguide, and by controlling the delay between the pump pulses, we can control on the fly the emission wavelength of the photons, while still inheriting all the record metrics of the IFWM scheme.

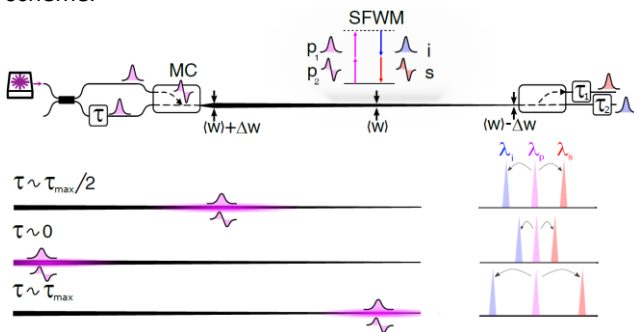


**Figure 5:** Top: sketch of the source, with indicated the relevant components and parameters (MC = Mode Converter). Bottom: principle of operation of the tunable source. The phase matching wavelengths of the Signal ( $\lambda_s$ ) and of the Idler ( $\lambda_i$ ) (right sketch) is tuned by changing the delay  $\tau$  between two pump pulses, making them to overlap in different positions (magenta color) along the waveguide.

As shown in Fig. 5, the delay determines the point where the pump pulses overlap, which in turn selects the segment of the waveguide where pair generation occurs. Since the Signal/Idler frequencies depend on the local waveguide cross-section, this reconfigures the generation wavelengths of the pair. This feature is used to recover the spectral indistinguishability in presence of fabrication errors.

We numerically show that, under realistic fabrication tolerances (device layer thickness uniformity  $< 1 \text{ nm}$ , waveguide width error  $< 15 \text{ nm}$ ), sources on the same chip have a pair-wise HHOM visibility which is only degraded by 0.35% from the case where they are identical. When the sources belongs to different dies, the difference in the device layer thickness could be higher. This scenario could be relevant for two distant quantum communication devices relying on single photons. Even in this case, we show that an indistinguishability level  $> 95\%$  can be guaranteed up to a difference in the waveguide height  $\sim 4 \text{ nm}$ , and for errors in the waveguide width larger than  $100 \text{ nm}$ . Under these circumstances, the degradation of the HHOM visibility is less than 3% of its value compared to the case of two identical sources. In comparison, the visibility and the indistinguishability will be both below 20% without delay optimization. The delay can be controlled on chip with thermo optic phase shifters, making the device suited for large-scale programmable silicon photonics quantum processors.

#### 4. A silicon photonics source of entangled photons for mid infrared ghost spectroscopy (M. Sanna, D. Rizzotti, S. Signorini)

Many applications in quantum optics rely on the two-photon state (biphotons) emitted by parametric sources. In our work, we investigate the application of intermodal spontaneous four wave mixing (SFWM) to quantum ghost spectroscopy (GS) in the mid-infrared (MIR) spectral region. This quantum technique is of great interest for MIR sensing, being able to overcome the limitations faced by MIR detectors in terms of background noise and dark counts. This spectroscopy method uses time-energy entangled photons, with one photon at the wavelengths interesting for the absorption spectroscopy, and the other photons at wavelengths easy to be detected. The idea of GS is to perform the spectroscopy analysis over the easy-to-detect photon, which carries the spectral information of the sample thanks to the spectral correlations due to entanglement. Interestingly, the application of this technique to MIR wavelengths allows probing the spectral fingerprints of molecules.

In our work, through intermodal SFWM in a Silicon-on-Insulator (SOI) waveguide, two temporally correlated photons are generated using a standard C-band pump: the idler photon around  $1300 \text{ nm}$  (near infrared (NIR)) and the signal photon beyond  $2 \mu\text{m}$  (MIR). The quality of the source is quantified in terms of coincidence to accidental ratio (CAR), which quantifies the probability of having a coincidence count due to the entangled photons instead of being due to noise. We measured a high maximum CAR,  $114 \pm 4$ . We used the integrated source to perform quantum GS of  $\text{CO}_2$ .

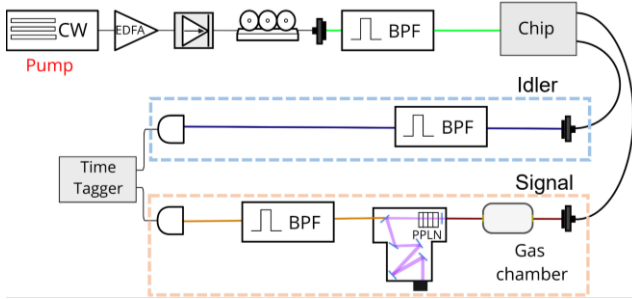


**Figure 6** Scheme of the experimental setup. A tunable continuous wave CW laser followed a laser filtering stage. After the SOI platform, the generated twin photons are collected by two different fibers, one for the idler photons and one for the signal photons. The idler channel (dashed blue line region) has a tunable band pass filter (BPF) and an InGaAs single photon avalanche detector (InGaAs SPAD). The signal channel (orange dashed line region) has a Gas chamber followed by an upconverter system coupled to a silicon SPAD after a BPF.

As shown in Fig. 6, the signal photon hits a bucket detector, after passing through the gas sample. The correlated idler photon passes through a band pass filter that selects the spectral resolution of the spectroscopy. The spectrum of the gas is measured by varying the wavelength of the pump, thus changing the wavelength of the probing signal photon and of the correlated idler, and by measuring the coincidences. Thanks to the coincidence detection, the background noise is greatly suppressed. This is a further advantage of this technique with respect to the classical spectroscopy. To demonstrate this, we introduced an artificial source of white noise in the signal channel, leading to a signal-to-noise-ratio (SNR)  $\ll 1$  for the signal beam.

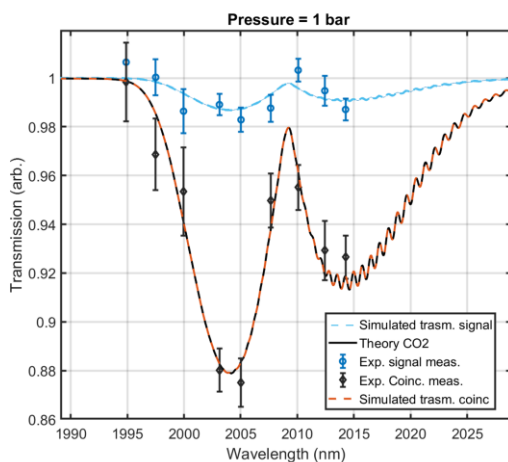


**Figure 7** Experimental measurements of CO<sub>2</sub> transmission spectra. Measurement with a cell filled with 1 bar of CO<sub>2</sub> a room temperature. The light blue line and dots are the simulated and experimental signal photon transmission as in a classical spectroscopy measurement. The red line and black dots are the result of a GS simulated and experimental measurement where the net coincidence counts are recorded as a function of the wavelength.

In Fig. 7, we report the spectrum of the CO<sub>2</sub> measured with quantum GS and with classical spectroscopy (the signal counts without coincidence). The quantum GS measurement (black dots) retrieves correctly the spectrum of CO<sub>2</sub> and exhibits a higher visibility for the spectral measurement with respect to the classical measurement (light blue dots), which barely resolves the CO<sub>2</sub> absorption band. The simulations (dashed lines) match the experimental measurements.

### 5. Min-entropy estimation of a QRNG based on single-photon entanglement for different levels of trustiness in the source (Stefano Azzini, Nicolò Leone)

Random numbers are important tools to guarantee, e.g., the privacy of communications between different parties. The min-entropy quantifies the number of effectively random bits present in a sequence. Here, we demonstrate a quantum random number generator (QRNG) based on Single Photon Entanglement (SPE). In this case, the min-entropy can be certified using a Bell's inequality, together with a partial characterization of the measurement schemes. The source is assumed to be stationary, but uncharacterized. The experimental implementation of the QRNG is shown in Fig. 8.

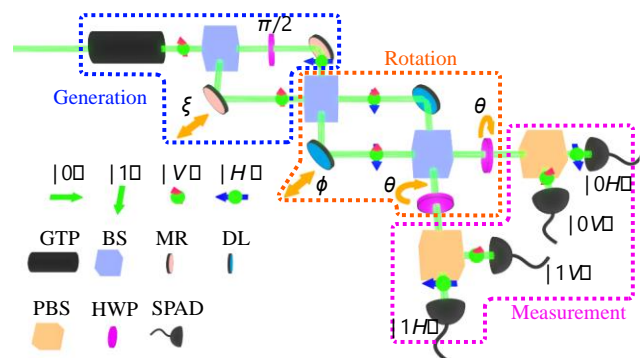


**Figure 8:** Scheme for the generation of quantum random numbers based on the violation of a Bell inequality with SPE states. The dashed boxes represent the generation (blue box), the rotation (orange box) and the measurement (pink box) stages. The optical path is represented by a green line, while single photons by a green sphere. The colored arrows represent the polarization of photons. The optical components involved are Glan-Thompson Polarizer (GTP); Beam Splitter (BS); Mirror (MR); Delay Line (DL), composed by three mirrors for optical alignment purposes; Polarized Beam Splitter (PBS); Half-Wave Plate (HWP); Single Photon Avalanche Diode (SPAD).  $\xi$  represents the angle used to compensate for differences of phase in the generation.  $\phi$  is the angle that fixes the direction of measurement for momentum,  $\theta$  is the angle that fixes the direction of measurement for polarization.

Our protocol is based on the knowledge of the optical properties of the beam splitters and the mirrors in the Mach Zehnder Interferometer (MZI, orange box in Fig. 8)

and on the characterization of the detectors (pink box in Fig. 8). The protocol works in the following way. First, an entangled state of the momentum and polarization degrees of freedom of single photons from a laser beam is prepared (blue box in Fig. 8). Then, the state is manipulated by properly selecting the phase  $\phi$  of the MZI (for momentum rotation) and the angle  $\theta$  of the two waveplates (for polarization rotation), located just before the measurement stage. The latter projects the manipulated state on the two-qubit basis  $\{|0V\rangle, |1V\rangle, |0H\rangle, |1H\rangle\}$ , where  $|0\rangle$  and  $|1\rangle$  represent the basis of the momentum qubit, while  $|H\rangle$  and  $|V\rangle$  the basis of the polarization qubit. Such an operation is repeated  $n$ -times for four couples of angles  $\phi$  and  $\theta$ . Once acquired all the measurement outcomes sequences, a CHSH Bell inequality is evaluated. The latter acts as a randomness witness: if the Bell's inequality is violated ( $|S| > 2$ , where  $S$  is the Bell correlation function), then a certain amount of randomness is present in our sequence and, to that extent, it can be used as a sequence of intrinsically random numbers. With no hypothesis on the form of the input entangled state, a min-entropy value of  $2.5 \pm 0.5\%$  is certified.

Let us define the maximally entangled state  $|\psi\rangle = \frac{1}{\sqrt{2}}(|0V\rangle + |1H\rangle)$ . Any deviation from this state  $|\psi\rangle$  decreases the produced randomness. When the deviation is caused by only imperfections of the optics in the generation stage, e.g., the half wave plates and/or the relative phase  $\xi$  (Fig. 8), a min-entropy value of  $6.3 \pm 0.5\%$  is obtained. If only the phase  $\xi$  is wrong, then the min-entropy is  $26.9 \pm 0.5\%$ . If the optics is set to the ideal values, the certified min-entropy increases up to  $30.1 \pm 0.5\%$ . Therefore, the introduction of assumptions about the source increases the min-entropy by one order of magnitude. It is important to note that introducing new assumptions introduces also possible non-robustness of the quantum random number generation protocol, exploitable by any adversary.

## 6. On-chip Bell test of single-photon entangled state (Stefano Azzini, Nicolò Leone)

The on-chip integration of practical semi-device independent quantum random numbers generators is of interest to guarantee unbreakable security, e.g., in Internet of Things applications. The violation of a Bell's inequality certifies the intrinsic randomness in a sequence of digits. To perform a Bell test in a photonic chip, we need to generate an entangled state and to measure its four expectation values. Since single photon entanglement (SPE) is well suited for low cost applications, we designed and test a photonic chip where SPE is generated in the momentum basis. Here, the entanglement is written between two different subsets of waveguides, which are conveniently treated as two distinct

degrees of freedom, i.e. two qubits showing a path entanglement. To grasp the idea behind this entanglement it could be easier to think about the set of the natural numbers. In such a set, it is possible to find disjoint subsets like the ones of the odd and even numbers, or even more unusual ones (e.g.  $\{1x\}$  and  $\{2y\}$ , with  $x$  and  $y$  natural numbers). Once detailed the desired subspaces, by construction it is possible to treat them as qubit spaces and, moreover, it is possible to define operators inside them. Going back to integrated photonics, structures like crossings (CRs), multi-mode interferometers (MMI) and Mach Zehnder interferometers (MZI) are needed to write the path entangled state and to perform the rotation operations necessary to test the Bell's inequality. In particular, one MMI and two phase shifters (PS, i.e. a heater on top of a waveguide) are required to write the desired entangled state, while four MZIs with two CRs perform the measurements. To observe a violation of the Bell's inequality a precise characterization of each optical element of the chip must be carried out. Figure 9 shows an example of the characterization curve of one MZI with the fit function  $Counts(W) = a \cos^2(bW + c) + d$ . The relation phase-power is then reconstructed using the coefficients  $b$  and  $c$  of the fit. This operation is repeated for each MZI present in the circuit.

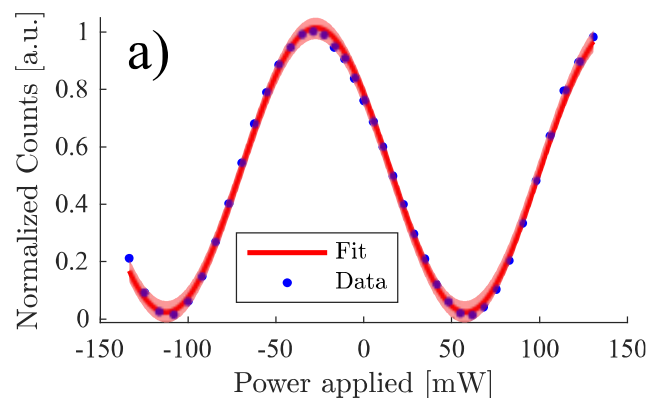


**Figure 9:** Characterization of an integrated MZI. The blue dots are the experimental data, while the red curve is the fit used to reconstruct the linear relation between the rotation angles (or phase) and the power dissipated on the heaters. Each MZI has two PSs, one for each arm. Note that, physically, the positive (negative) sign on the power corresponds to having applied the current to the first (second) PS.

Calibrated the phase-power relation of each integrated MZI, a Bell test is performed, as outlined for the experiment in Fig. 9. The signals are detected off-chip using four fiber-coupled single photon avalanche diodes (SPADs), monitored by a time tagging electronics. To perform a Bell test, four angles ( $\phi_1, \phi_2, \theta_1, \theta_2$ ) are chosen to select the four observables that have to be measured on the produced entangled state. In addition, the correlation between the different expectation values are evaluated by constructing the correlation coefficients  $S$ . If the absolute value of the correlation coefficient  $S$  results to be greater than 2 then the state is entangled. We have experimentally

reported a considerable violation of the Bell's inequality:  $S = 2.39 \pm 0.02$ ;  $S = -2.32 \pm 0.02$ ;  $S = 2.731 \pm 0.005$ ;  $S = -2.689 \pm 0.007$ ;

Such obtained  $S$  correlation function violations are achieved by selecting different observables by changing the angles ( $\phi_1, \phi_2, \theta_1, \theta_2$ ) and by writing an entangled state of the type  $|\psi\rangle = 1/\sqrt{2}(|A0\rangle + |B1\rangle)$ , where  $|0\rangle$ ,  $|1\rangle$  refer to one subset of waveguides, while  $|A\rangle$  and  $|B\rangle$  to the other subset of waveguides, each one corresponding to a momentum basis suitably defined within the photonic circuit. These obtained violations are preliminary results; a more careful evaluation of the setup non-idealities has to be carried out.

### 7. A single microring resonator as reservoir computing network: isolating the device response for nonlinear and memory tasks (Davide Bazzanella, Stefano Biasi, Mattia Mancinelli)

Reservoir computing is an intriguing technique to put into effect artificial neural networks in hardware. It achieves an interesting trade-off between training difficulty and performance, exploiting complex physical phenomena. We investigate the nonlinear response of a ring microresonator used as a reservoir computing network, via the time-multiplexing method. The computing and memory performance is graded for several tasks, linear and nonlinear, for numerous combinations of power, frequency, and bitrate. This emphasizes the importance of identifying the performance of the device alone, possibly by comparing input and output signals.

The nonlinear response of a microresonator follows the temperature and free carrier dynamics, which are influenced by the optical energy stored in the cavity. The response for a time varying optical signal, such as a pseudo-random binary sequence (PRBS), will depend on the current input and the existing state, caused by the past input. The device fading memory and its computing performance are evaluated experimentally by training an off-line ridge regression model on the traces sampled from the output optical signals. The ridge regression model is fed with samples from windows containing a different number of bits, in order to compare their performance. The tasks that the system must perform are the AND (linear) and the XOR (nonlinear) logical operations, between delayed bits.

In order to isolate the actual performance of the device, the same training is carried out for the optical signal at the input. In this way, distortions due to the optical modulator, the amplifiers, and/or the detection technique can be assessed and taken into account when observing the final performance. This operation is crucial for the case of the virtual node approach, especially as the off-line training is much more sensitive to small features and thus more likely to suffer overfitting.

The results for linear tasks show that the system is able to produce memory of 1 bit in the past for almost every combination of the parameters of the input signal. Moreover, a restricted set of parameters is found optimal for proving a memory of 2 bits in the past. However, no combination of parameters is able to yield three or more bits of memory. These results are substantiated by the analysis of the performance improvement over the input signals, which isolates the performance of the device alone. The performance improvement of the device usually arises for bitrates having a timescale of the same order of magnitude as the one associated with free carrier effects.

The results for the nonlinear task show an even more interesting situation. Indeed, the XOR operation between delayed bits requires both memory and nonlinearity. When the two bits are adjacent, the system is able to solve (error free) the task in a set of combinations only when the regression is fed with both bits. The same mechanism is even more visible for the delayed XOR between bits separated by an extra bit (XOR2), as shown in Fig. 10.

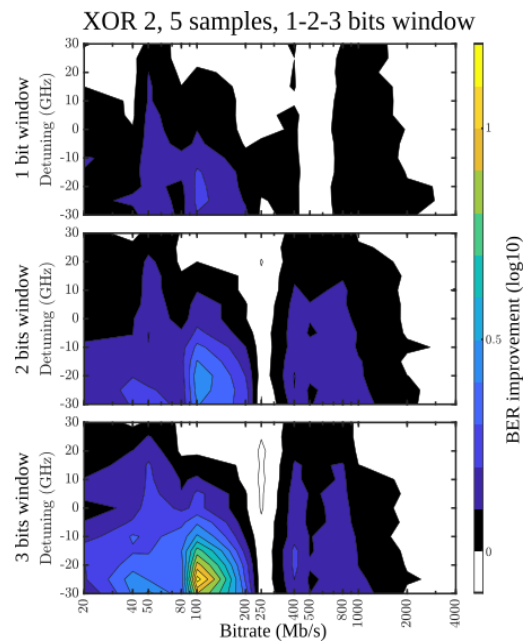


**Figure 10:** isolated BER improvement due to the device for the delayed XOR task carried out between the current bit and the one two bits in the past. The contour plot is in  $\log_{10}$  and the color map is in grayscale (white and black) for regions showing performance degradation and colored (blue-green-yellow) for regions showing performance improvement. The three graphs are obtained by changing the number of bits fed to the ridge regression.

In conclusion, we tested an add-drop microring resonator employed as a reservoir computing through the time-multiplexing approach. We noticed a connection between the bitrates of best performance and the timescales associated with nonlinear (free carrier) effects. Furthermore, we studied the effect of the bit window of the regression in the case of nonlinear tasks (XOR).

## 8. Silicon microring resonator in time delay reservoir computing (Giovanni Donati)

The role of a silicon microring resonator (MRR) as a computational unit in a time-delay reservoir-computing scheme is numerically studied. In this approach, the MRR is coupled to an external optical feedback and the response of the system is exploited for computation. Specifically, we investigated the case where the feedback line connects the through and the add ports of the MRR.

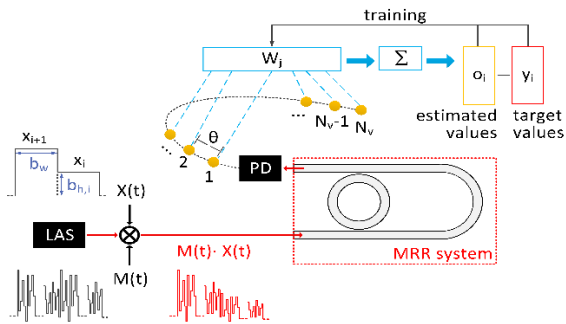


**Figure 11:** Schematic of time delay RC with an MRR subject to optical feedback. The encoded information  $X(t)$  is masked with a sequence  $M(t)$  and modulates the optical power from the laser (LAS) emission. At the drop port, the photodetected (PD) signal provides the time-multiplexed output states of the reservoir, which are weighted and linearly combined to compute the predicted value  $o_i$ . The weight optimization is performed via a linear classifier, with supervised learning over the expected values  $y_i$  data set.

The delay time of the external feedback determines the clock of the device, as every input bit to process is stretched in time to match it. The nonlinear transformation of the system, needed for computation, is carried out by the MRR free carrier nonlinearity and by the photodetection square law. While this last always applies, as we detect the drop signal, the former one depends on the optical power circulating within the MRR while computing, which in turn depends on operating and design parameters. To guarantee a relevant free carrier nonlinearity, the MRR modelled has a quality factor  $Q = 3 \times 10^4$  and can exhibit self-pulsation dynamics, a phenomenon that relies on a free carrier concentration variation in the waveguide.

We studied the versatility of this device, by exploiting both the linear and nonlinear MRR dynamics and we tested it in computing tasks with diverse memory requirements. We observed that when large memory is required, as it occurs in the Narma 10 task, the best choice is to operate the MRR in a linear regime with high feedback strength: this allows the feedback signal to iterate multiple times through the system, contributing as an optical source of linear memory during the task. The square detection is the only nonlinearity of this processing scheme. On the contrary, for computing tasks such as the Mackey-Glass and the Santa

Fe chaotic time series prediction, the MRR and the photodetection nonlinearities contribute both to efficient computation. In particular, three processing schemes are available to better fit a tasks: i) Linear MRR and feedback, ii) Nonlinear MRR and feedback, and iii) Nonlinear MRR in absence of feedback.

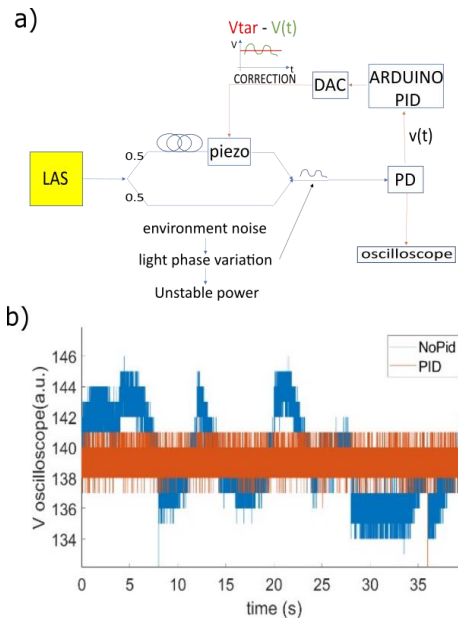


**Figure 12:** a) PID scheme: a photodetector (PD) at the end of an interferometer sends an electric signal  $V(t)$  to Arduino, where it is compared with a target constant signal  $V_{tar}$ . A digital to analog converter (DAC) drives the correction signal to the piezo-driven phase shifter. b) Output signal of the interferometer with/without the PID controller.

These modelling results are propaedeutic to an experimental investigation. As we use an optical fiber to realize the feedback line, a first problem to face is the stabilization of the feedback signal: thermal, vibrational and phonic noise affect the phase of the feedback signal, resulting in a noisy interference with the MRR optical field. To compensate for these fluctuations, a PID controller has been realized using a piezo-driven fiber stretcher, driven by an Arduino Mega. This controller was tested with a scheme illustrated Fig. 12. By stretching the fiber in a controlled way, the induced phase variations in the optical signal can compensate the ones induced by environmental noise, resulting in a stable output optical signal.

## 9. A feed forward network with microresonators as neural activation function (Stefano Biasi, Riccardo Franchi, Davide Bazzanella, Marco Peretti)

In the last decade, new machine learning methods have been developed. Their application has led to the solution of complex tasks, such as object recognition or board games, with performances that are often better than the

human ones. Among the distinct approaches, the nonlinearity of the network's nodes, either their activation function or their fading memory, plays a crucial role in defining the final performance.

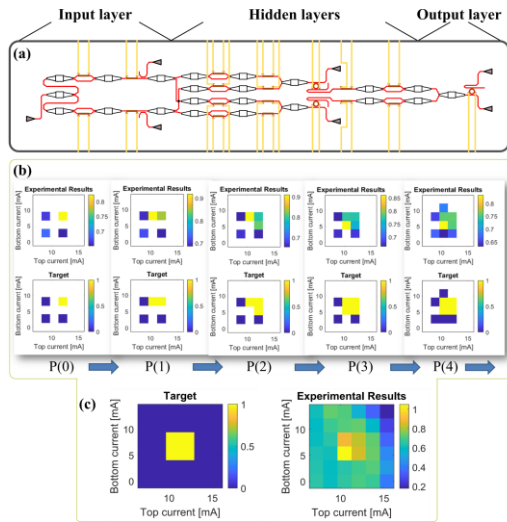


**Figure 13:** (a) Design of the feed-forward neural network. It consists of four stages: an input layer in which the information is encoded, two hidden layers where the input data is processed, and an output layer to acquire the network's response. Panels (b) and (c) show the comparison between the experimental results and the prefixed theoretical target. All the graphs display the intensity of the output field as a function of the currents applied on the MZIs of the input layer.

We propose a feed-forward network, which allows solving tasks with at most two input signals and only one output. It is integrated in a Silicon on Insulator (SOI) platform, and the encoding of the information as well as the signal processing take place within the chip. The network's nonlinear activation functions are ensured by three microresonators in add and drop configuration. Figure 13 (a) shows the scheme of the feed-forward network. It can be divided into an input layer, two hidden layers, and an output layer. In the input preparation layer, an incoming coherent beam is divided into two and the information is encoded by controlling both the amplitude and the phase of the incoming field. This control of the signal is performed by means of two nearly-balanced Mach-Zehnder interferometers (MZIs) and two phase shifters (PSs), which are thermally controlled. The encoded information enters into the first hidden layer where it is further divided and it is weighted through a cascade of MZIs and PSs. The resulting signals excite two microresonators via their input port. Then, their drop port signals pass into a second hidden layer where it is further subjected to a linear combination via a modulation of either amplitude or phase. Finally, the signal enters

into a third microresonator via the input port and its response at the through port represents the output signal of the network. Note that since the through and drop ports are closely related by the energy conservation, the final output consists of a single signal.

The training of the network consists in determining the values of the currents to be applied to the heaters placed in the hidden layers. Specifically, thirteen current values are regulated. These currents are applied on the MZIs and PSs and to the three microresonators. These latter currents allow changing the resonant frequency in order to fully exploit the nonlinear response. The training of the feed-forward network is achieved in a supervised learning method by minimizing a cost function through a gradient free algorithm. Precisely, the target is split into several chained-tasks in order to decrease the learning time and to guide the network to the final goal. We solve different nonlinear tasks by reproducing, on a six by six pixels matrix, distinct shapes such as a square, an "L", an "O" and a "Z". This matrix is created by discretizing the input field intensity. Figures 13 (b) and (c) show the comparison between the results of the experimental measurements and the prefixed theoretical targets. Specifically, panels (b) show the chain-like division capable of solving a square on the input grid (see panel (c)). All the graphs show the intensity of the output field as a function of the current applied to the heater of the MZIs placed into the input layer. The bottom panels display the theoretical target while the top ones display the experimental measurements. For the  $i$ -th task a cost function is minimized in order to determine the ideal parameters  $P(i)$ , which are then used as initial conditions for the resolution of the  $i$ -th+1 task. The study of the currents applied by the training process shows that the role of the microresonators is crucial for the solution of the nonlinear tasks.

## 10. Training and learning in ALPI (Mattia Mancinelli, Emiliano Staffoli)

The ALPI project aims to develop an integrated Photonic Neural Network (PNN) for all-optical signal recovery from the distortions induced by the optical propagation in a fiber. A proper training method has to be chosen. The Adam algorithm has been investigated as a faster alternative to gradient-free minimization algorithms, such as the Particle Swarm Optimizer (PSO). Its name derives from *Adaptive Moment Estimation*, alluding to the fact that it exploits the estimates of the first and second moments of the gradient for the generation of an adaptive step for each of the tunable parameters. A distinctive characteristic of Adam is that the descent proceeds with a memory of the previous iterations, since the present step is proposed by taking into account the history of the descent itself. The amount of

memory that the algorithm has to keep trace of is determined by a mean of the parameters  $\beta_1$  and  $\beta_2$ , being these the exponential decay rate for the moving averages. The introduction of memory allows proceeding the descent towards the minimum even when noise does not allow for a precise estimation of the gradient.

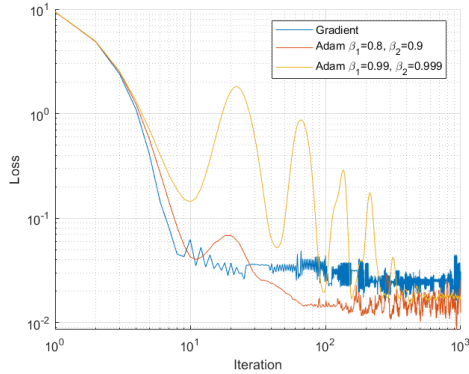


**Figure 14:** Loss function minimizations performed with the simple gradient descent and the Adam algorithm in two memory configurations.

Figure 14 shows simulated results of the minimization of a noisy loss function performed in two memory configurations. The modelled neural network aimed to estimate the distance between an input vector and a reference one in a 10-dimensional space. It is shown that the introduction of memory allows overcoming the limitations imposed by noise on the gradient descent. Note also that inducing too much memory in the descent is counter-productive: indeed, the inertia induced in the system could become sufficiently high to induce a deviation from the straight path to the minimum. The proper compromise has thus to be found for each problem.

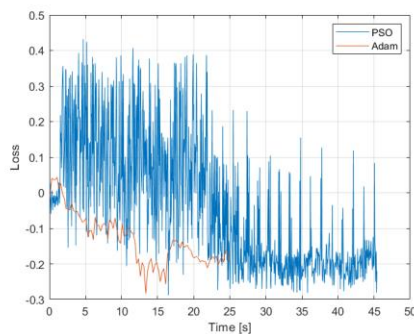


**Figure 15:** Minimizations performed in an experimental context with the Adam algorithm and the PSO provided with the same starting point. The loss function is associated to a complex perceptron adopted as PNN for in the context of signal recovery. For the minimization reported above, the signal travelled in a 75km fiber span.

The performances of Adam and the PSO have been compared in an experimental context. A 4-channel complex perceptron was employed as a PNN for all-optical signal recovery after propagation in fiber, as a preliminary study for the future ALPI device. Figure 15 reports the comparison

between the minimizations of the relative loss function performed with the Adam algorithm and the PSO. With the loss estimates being comparable, time time-saving related to Adam is evident. The aim for the future is to test the performances for the Adam algorithm with a more complex photonic neural network involving a higher number of parameters.

### 11. Intersymbol interference as a technique to measure memory in a neural network (Mattia Mancinelli)

One of the goals of the BACKUP project is to demonstrate a way to achieve optical memory through a cascade of coupled microresonators. Here we report the study carried out on the device of Figure 16. We modified a SCISSOR by looping the through and add ports and by adding optical delay lines between each ring. The device is equipped with spirals whose nominal delay is 25 ps (D).

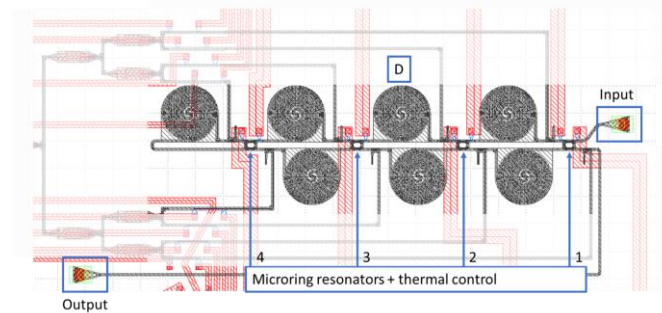


**Figure 16:** Device under test composed of a sequence of 4 resonators in a SCISSOR like configuration with interposed delay lines made by spiral waveguides and looped through and add ports. Thermal controls in each ring are also available. Spiral's delay is 25 ps.

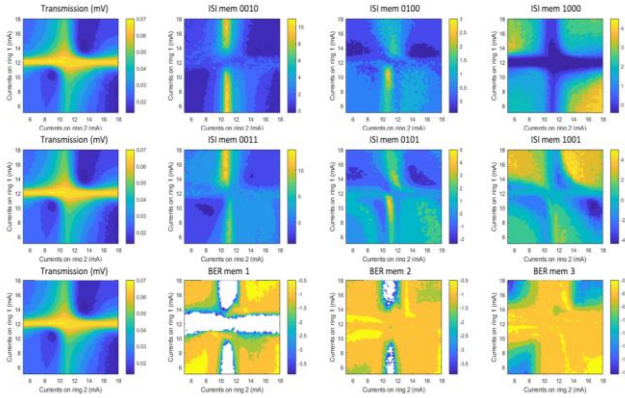
In this configuration, the rings act as tuneable mirror that can be used to select the optical path between input and output and so the device memory. We developed a fast method that exploits intersymbol interference (ISI) to estimate not only the magnitude of the linear memory but also its phase. The method probes the system by sending a series of isolated pulses (or bit).

The experimental results are reported in Figure 17 when the heater current on ring 1 and 2 is swept from 5-18 mA. The resonant currents for the first two rings are 12 mA and 11 mA respectively. Rings number 3 and 4 are tuned so they are out of resonance to ensure a reduced space of parameters to be scanned. The input power is kept below the non-linear threshold of the microrings since the method can estimate correctly only linear memory. The memory is provided by the number of spirals involved in the optical path, which can be modified by the add-drop function of the tuneable micro-rings.

Depending on the thermal tuning applied on the first 2 resonators four main behaviours are expected:

1. Minimum memory when first ring is resonant

2. Maximum memory provided by 7 spirals when all resonators are out of resonance
3. Memory provided by 2 spirals when the second ring is resonant
4. A mixture of the previous 3 points driven by the applied thermal tuning.



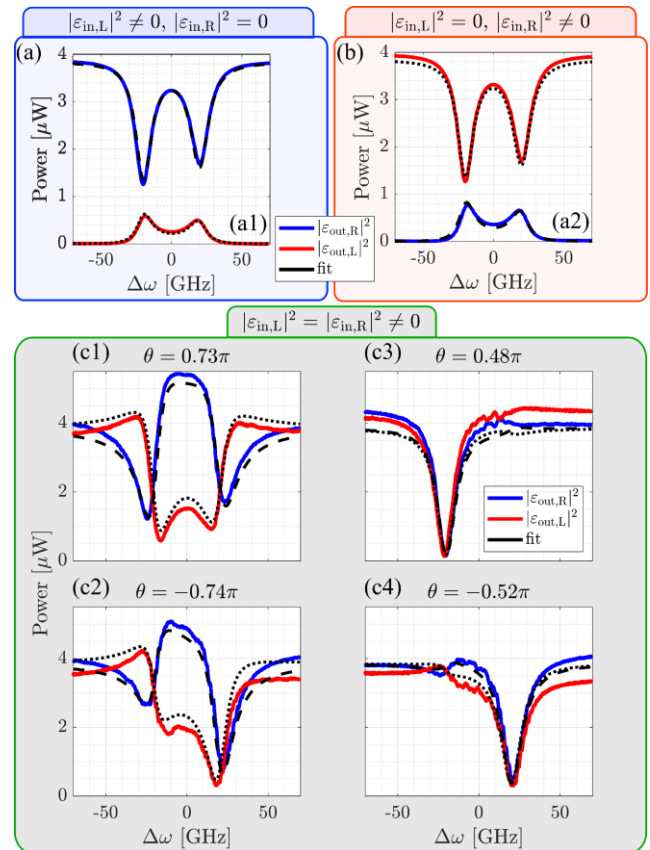
**Figure 17:** Experimental results

Figure 17 reports several panels representing the DUT transmission and the SNR resulting from the ISI test. The transmission map highlights the regions in which resonance occurs because high transmission corresponds in general to low loss and so short path. The amount of transmission is linked to the amount of memory by the losses. The yellow horizontal line corresponds to the resonance of the 1<sup>st</sup> ring, the vertical one to the resonance of the 2<sup>nd</sup> ring while the area in between to a mixture of these 2 cases. The presence of recurrence is seen in the deep blue areas located near the resonance of the 2 rings (CRIT). The SNR shows high value along the vertical line related to the resonance of the second ring.

The phase of memory can be extracted by comparing the SNR maps of Figure (a) to those in Figure (b). As an example, we can see that for the pattern 0010 the maximum SNR is symmetric around the ring 2 resonances while for pattern 0011 the symmetry is lost. When the 1 is added at the reference time, phase sensitivity is enabled because we are observing the sum of two complex quantities. A resonator provides a phase shift that is related to the sign of the detuning. This means that a change on the detuning will affect the complex sum of the two ones resulting in an asymmetric map. The ISI results are confirmed by the memory test, shown in Figure (c), performed using the virtual nodes approach. Here we train the system to reproduce a delayed copy of the input and bit-error-rate (BER) is used as a figure of merit. Areas with low BER are correlated to areas with high SNR.

## 12. Coherent interferometric excitation to study Hermitian and Non-Hermitian system (Stefano Biasi, Riccardo Franchi, Filippo Mione)

The modeling of natural phenomena often requires the study of a specific subsystem and its interaction with the surrounding environment in the framework of non-Hermitian physics. Since the propagation of light is typically affected by losses, optics is a fertile ground for studying these systems. Commonly, the non-Hermitian Hamiltonians are built by exploiting optical devices, which allow the interaction between two propagating modes, such as coupled microcavities, or a Tajiri microresonator. These structures are typically described by a two-level system in the mathematical framework of the temporal coupled mode theory. Consequently, the knowledge of the eigenvalues and eigenvectors represent a fundamental aspect.



**Figure 18:** Experimental results for a microring. Panels (a) and (b) show the transmitted and reflected intensities as a function of detuning frequency for a single-side excitation from the left and right facet, respectively. Panels (c1)-(c4) show the output field intensities as a function of detuning for an interferometric excitation characterized by the same amplitude as the two input fields. Precisely, (c1), (c2), (c3), and (c4) report the responses for a phase equal to  $\vartheta=0.73\pi$ ,  $-0.74\pi$ ,  $0.48\pi$ , and  $-0.52\pi$ , respectively. The blue (red) lines refer to the field strengths exiting from the right (left) side, while the black lines are the fits with our analytical model.

We propose and validate a novel technique, which allows estimating directly from the spectral measurements the eigenvalues of either Hermitian or non-Hermitian optical devices. This method is based on the simultaneous coherent excitation of the counter-propagating modes. In particular, we make use of an interferometric excitation to study a simple microring and a Taiji microresonator. In the first case, the coupling between the modes is due to the surface-wall roughness, and therefore, to the photon backscattering which excites the other mode. In the second, the modal coupling is due to a S-shaped waveguide embedded in the microring. We demonstrate theoretically and experimentally that the complex nature of the eigenvalues can be studied by varying the amplitudes and the relative phase between the two incoming counter-propagating fields. Figure 18 shows the output fields from a microresonator affected by backscattering as a function of the detuning frequency with respect to the resonant frequency. In particular, panels (a) and (b) show the typical doublet response to a single-side excitation from the left and right facets, respectively. The blue (red) lines highlight the field exiting from the right (left) facet, while the black ones are fit with our analytical model. The Lorentz reciprocity theorem ensures the same transmission response, but the non-Hermiticity of the system induces two different reflections. Panels (c1)-(c4) show the intensities of the output fields for a symmetric interferometric excitation (i.e., with the same intensity of the two incident beams) with different values of the relative phase between the input fields. The variation of the phase gives rise to different spectral responses. In the case of  $\theta = \pm\pi/2$  the typical transmission doublet merges into a single Lorentzian. Its resonant frequency is the real part of the eigenvalues. On the other hand, its full width at half maximum is closely related to the imaginary part of the eigenvalues. Furthermore, this collapse allows estimating the quality factor of a microresonator in the absence of backscattering. Finally, we show that a Taiji microresonator works on an exceptional point and we report a direction-dependent response due to the interferometric excitation.

### 13. On the response of the Taiji microresonator against small perturbation on its exceptional point (Riccardo Franchi, Stefano Biasi, Filippo Mione)

The Taiji microresonator is characterized by an embedded S-shaped waveguide, see Fig. 19(a). The Taiji is a non-Hermitian system that behaves as a unidirectional reflector. In fact, the S-shaped waveguide couples the clockwise and counterclockwise modes of the microresonator only in one direction. Let us define the coupling coefficient  $\beta_{\text{Taiji}}$ . We have shown that a Taiji microresonator works on an exceptional point (EP). In fact, not only the eigenvalues are degenerate, but also the eigenvectors of the system coalesce. Hence, the Taiji eigenvalues have a square root behavior as

a function of a small Hermitian perturbation ( $\delta\beta$ ) to the modal coupling coefficients ( $\beta_{\text{Taiji}}$ ). Since normal microrings, working on a diabolic point (DP: coincident eigenvalues and orthogonal eigenvectors), respond linearly to small perturbations, we obtain that Taiji microresonators exhibit higher sensitivity, Fig. 19 (c).

Figure 19 (c) shows that the real part of the splitting of the eigenvalues presents a square root dependence in the Taiji case (red line), while it has a linear dependence with a lower slope for a simple microresonator (blue). This is confirmed by the modulus of the inner product between the two eigenvectors which is always zero in the case of a diabolic point, while it is 1 and decreases as the perturbation increases for the exceptional point case.

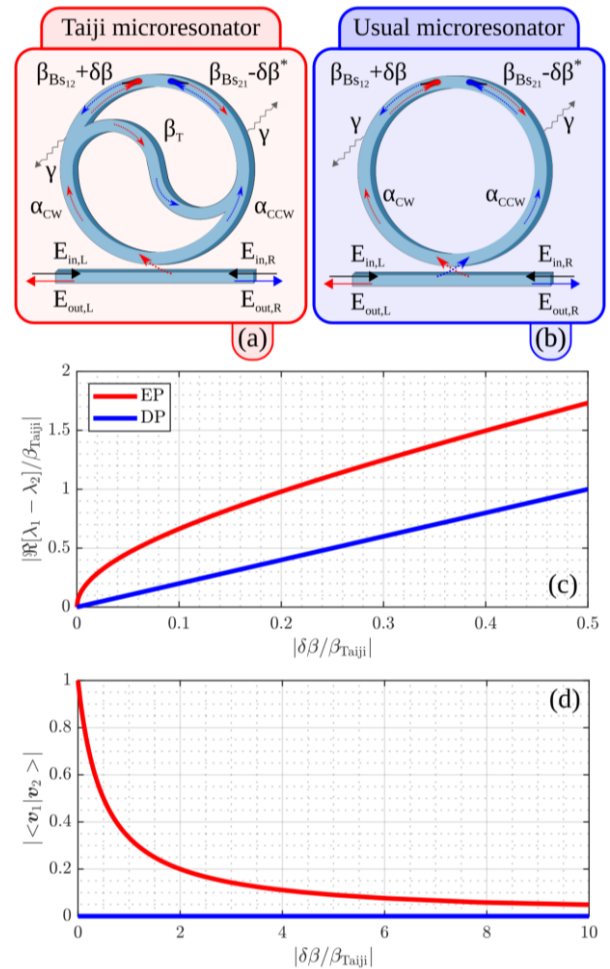


**Figure 19:** Panels (a) and (b) report the sketch of a Taiji and a usual microresonator. Panel (c) shows the real part of the eigenvalues splitting for the Exceptional (red) and Diabolic (blue) points as a function of a Hermitian perturbation of the coupling terms. In panel (d) the red and blue curves describe the behavior of the modulus of the inner product of the eigenvectors for the Exceptional and Diabolic points, respectively.

The first step to observe this phenomenon experimentally is to fabricate Taiji microresonators that exhibit both a high quality factor and a large difference between the two coupling coefficients of the counterpropagating modes

( $|\beta_{12}| \gg |\beta_{21}|$ ). Through experimental measurements, see Fig. 20, we demonstrate that it is possible to fabricate semi-ideal integrated silicon Taiji microresonators having quality factors  $Q$  lower than  $10^4$ . In fact, in this region  $|\beta_{12}| \gg |\beta_{21}|$ . Instead, by increasing the  $Q$ -factor above  $5 \times 10^4$ , i.e. decreasing the intrinsic and extrinsic losses ( $\gamma$  and  $\Gamma$ ), the taiji no longer works on an Exceptional Point because  $|\beta_{12}| \approx |\beta_{21}|$ . This is shown in Fig. 20 and is due to the presence of the surface-wall roughness. Such an effect is almost constant as a function of the  $Q$ -factor and at high  $Q$ -factor is predominant over the coupling given by the S-shaped waveguide.

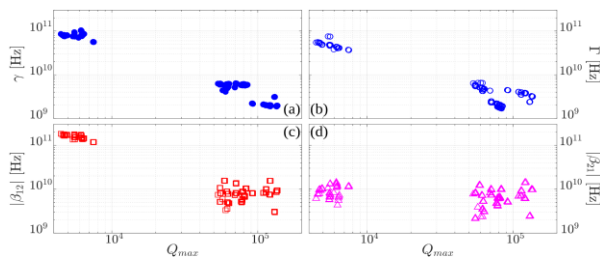


**Figure 20:** Panels (a), (b), (c) and (d) report the intrinsic, extrinsic and the two counter propagating mode coupling coefficients ( $|\beta_{12}|$  and  $|\beta_{21}|$ ) as a function of the maximum quality factor deduced by a fit of 180 Taiji microresonator resonances.

#### 14. Light induced activation of an in vitro neuronal engram (Beatrice Vignoli, Clara Zaccaria, Asiye Malkoc)

The term memory refers to the storing of knowledge that can be recalled by the brain. It is commonly assumed that information is stored in the brain as physical lasting alterations of a group of neurons, known as an engram. These permanent modifications include the reinforcement of synaptic connections (long-term potentiation and depression, LTP and LTD) and/or the increase in the number of spines among a specific set of neurons during memory trace encoding. One of the goals of the BACKUP project is to use patterned light illumination to generate a memory engram in a small in vitro neuronal network. The idea is to create this artificial engram utilizing optogenetic technologies in which light illumination will imitate the activation of a group of interconnected neurons expressing Channel rhodopsin along the light path. In this way, patterned light will function as an artificial learning event for the generation of memory engrams.

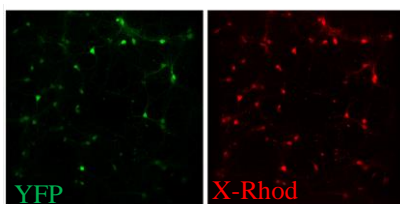


**Figure 21:** left panel shown neuronal culture infected with AAV-Chr2-YFP, middle panel shows x-Rhod indicator.

We implemented our setup with Digital Light Processing (DLP, LEDs, optics and WXGA DMD) to generate patterned illumination with custom patterns and single neuron resolution. We used DLP to stimulate embryonic hippocampal/cortical neuronal culture infected with Channelrhodopsin (pAAV-Syn-Chr2(H134R)- YFP). To track the responses of the network following Chr2 activation we used the fluorescent calcium indicator X-Rhod AM (Fig. 21). Experiments were performed exciting the X-Rhod indicator with the green line of the microscope and collecting the red signal of the indicator in the camera. The blue excitation light coming from the DLP goes into the rear entrance of the microscope and is projected down to the sample thanks to a dichroic mirror that acts like a high pass filter at 505nm. The excitation was performed illuminating with 45 pulses of 20ms with 3Hz frequency. To avoid artifacts recording, the camera and the DLP were triggered in such a way that the camera acquires only when the illumination is turned off. Multi-tiff images were acquired in order to follow the fluorescent signal of the calcium indicator during a stimulation event.

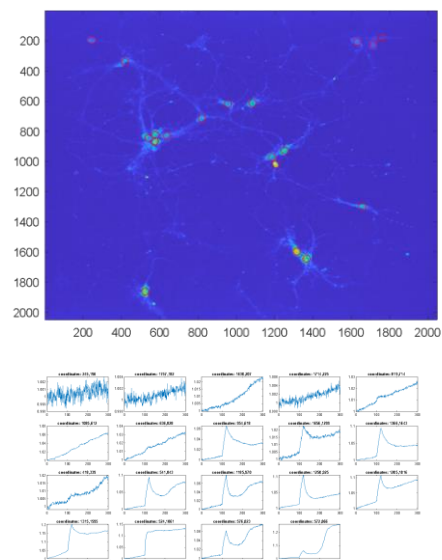


**Figure 22:** An example of analysis performed on a Multi-tiff image of a neuronal culture. Circles localize the recognized cell bodies. On these regions calcium fluorescence levels along all the frames are collected as calcium traces. Spikes in these traces represent a calcium event

To study the calcium responses, we wrote a Matlab code able to load the multi-tiff images, localize neurons and study the calcium traces in time in terms of intensity of the response and shape of traces (Fig. 22). The localization of neurons was performed on an image resulting by the average of the frames before the light excitation. A binarization of this image was performed using different pixel intensity values: doing so, different ROIs (neurons) were located and characterized using Matlab function “regionprops”, which

returns the centroids, areas and other geometrical parameters of the located region. These regions are then filtered by an empirical range of area values and geometrical shapes of neurons. During this procedure, an interactive section with the experimenter is included, to avoid the program to locate ROIs that are not neurons. The raw traces, the positions of the ROIs and the position of the light illumination stimuli allow performing the desired analysis of calcium network responses following a given stimulation. In order to test the possibility of activating only specific neurons of the network, we use a patterned illumination targeting only the cell bodies and we check the calcium activity of the stimulated neurons to confirm neuronal activation by spot illumination.

It is widely accepted that synapses between engram cells are formed or strengthened because of learning event. To test if our in-vitro engram displays this feature we took advantage of SynActive (SA) technology, a strategy developed to tag and map the synaptic connections in an input-specific manner. By combining RNA targeting elements with a targeting peptide tag, this innovative method enables for the production of specific proteins (i.e. HA) precisely at active synapses. We co-transfected hippocampal and cortical neurons with SA (TreP-Arc3'-Nend-PSDTag-Venus-HA-Arc5'UTR) and rtTATomato (CAG-rtTA-IRES-TdTomato) and we infected them with Channelrhodopsin. We demonstrated that LTP-like -light stimulation (10 trains of 13 light pulses at 100Hz repeated at 0.5 Hz) of 2 neuronal bodies simultaneously is able to induce activation of synapses as demonstrated by the increased number of spines expressing HA (HA+) following light stimulation compared to non-stimulated one (Fig. 23). This can be considered the first step for writing an engram in vitro.

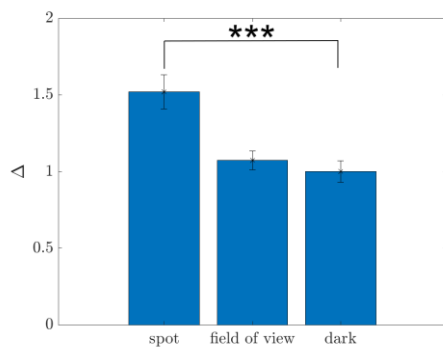


**Figure 23:** LTP analysis on spot excitations. The bar graph shows the  $\Delta$  values got on the cells excited with spot illumination ( $N=7$  FOV), on cells in the same field of view ( $N=7$  FOV), but not illuminated and on cells far from the field of view (dark) ( $N=26$  neurons). Data are average  $\pm$  standard error. \*\*\* $P<0.001$ , unpaired T-test.  $\Delta$  is defined as the number of HA+ spines in analyzed cells normalized over the number of HA+ spines detected in control cells (dark).

### 15. Statistical modeling of complex neural networks (Paolo Bettotti, Gianmarco Zanardi)

Neural networks (NN), in particularly recurrent ones, show

complex dynamics that is still poorly investigated and understood. Yet, their understanding is of paramount importance to exploit NNs full potential. This knowledge is even more important in photonic NNs where physical and technological constraints require a careful optimization of the number of nodes and of their organization. We recently started a research activity, in collaboration with prof. Luca Tubiana of the Statistical and Biological Physics group, aimed to develop statistical models able to capture the main features of complex NNs. The unveiling and understanding of key parameters describing the global behavior of NNs are fundamental to lay the groundwork for proper design of photonic (recurrent) NNs.

### 16. Characterization of in-vitro neuronal activity with electrophysiological signals (Ilya Auslender)

The goal in this study is to use neuronal electrophysiological signals to characterize the functionality of in-vitro neuronal culture. In particular, as part of the BACKUP and ISLAND projects, we aim to use this technique to read induced memories (engrams) in the culture. The measurement is performed by sampling and recording electrical signals from neurons cultured (in-vitro) on microelectrode array (MEA). After the preliminary processes of signal filtering and action potential (“spike”) detection are performed, we use the produced spike trains to analyze the activity recorded from the culture.

First, we characterize the culture by its spontaneous activity, i.e., a recording of neuronal activity without any applied stimuli. This allows us to explore the functionality and the connectivity of the cultured neurons. One of the indications of well-formed network is the existence of network bursts. Bursts are high-frequency spike trains which are typical in growing in-vitro cultures (Fig. 24). Typically, they occur in episodes, separated by silent phases. Network bursts are bursts that occur simultaneously (or with a short delay) at different sites of the network, which might also be synchronous.

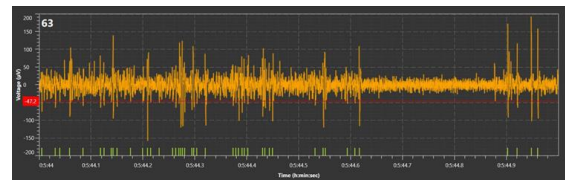


**Figure 24:** An example of recorded electrical trace containing bursts.

By analyzing the signals, we performed burst detection using a designated algorithm, which considers the inter-spike intervals. Using this data, we characterized the culture by its burst rate, which gives an indication about its maturity and functionality (Fig. 25).

Using the bursts data, we can also study the connectivity of the network at a large-scale level, i.e., between different

MEA channels, which can represent connections between different ensembles of neurons. This can be done by cross-correlation analysis between spike trains (or bursts) occurring in adjacent time windows. We have used an algorithm to analyze this type of functional connectivity in the culture. Figure 26 shows the outcome of the cross-correlation analysis on MEA map plot and depicts the strength (evaluated by cross-correlation amplitude) of connections between different MEA channels.

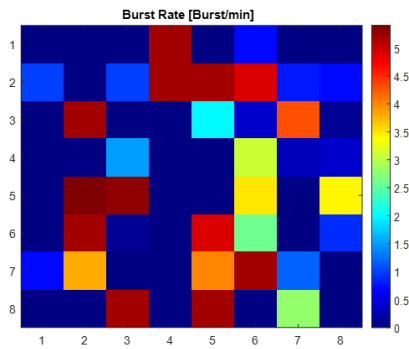


Figure 25: Map of average burst rate of a culture.

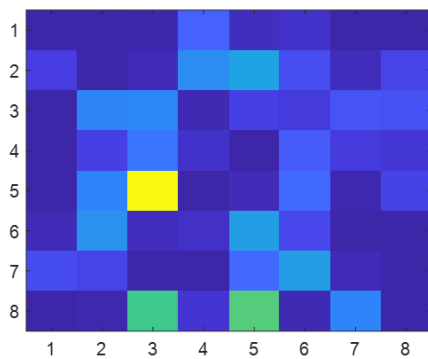


Figure 26: Cross-correlogram map, indicating the average correlation amplitude between the source signal electrode (indicated in yellow) and the other electrodes.

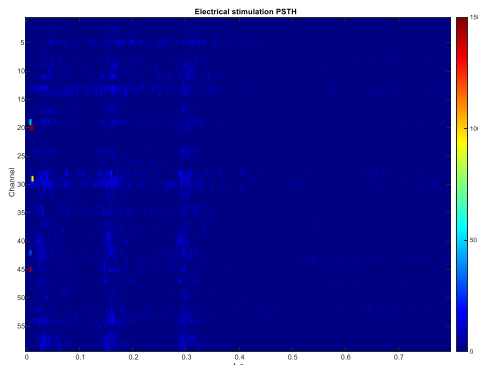


Figure 27: Post-stimulus time histogram (PSTH), showing the average response of each channel to stimulation at time  $t=0$ . Bin Size = 4ms.

We also performed measurements of evoked activity following electrical stimulation. At the first step we used test stimulation, which is a low frequency stimulation- 1 pulse every 5s. The response of the culture is measured by a spike histogram averaged over all the stimuli. This histogram is known as post-stimulus time histogram (PSTH) and shown in Fig. 27. As can be seen in Fig. 27, the response of the network comes in 2–3-time phases after the stimulation at time  $t=0$  followed by a silent phase at  $t\sim 350$ ms. To quantify the total response of the network per electrode, the signal of each channel is integrated over time and the result is shown on MEA map (Fig. 28). Next, we will carry out electrical tetanic stimuli, which are high frequency stimuli (5Hz or higher) in order to study long-term potentiation (LTP) using some of the analyses mentioned above.

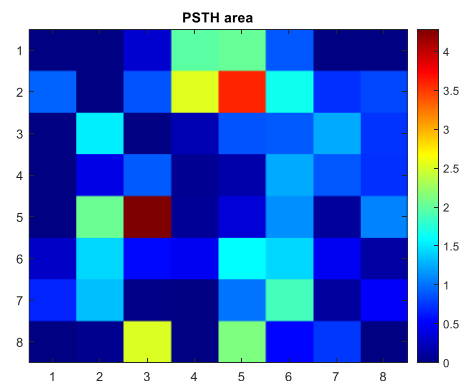


Figure 28: Map of total response of each electrode to electrical stimulation. The yellow lightning symbol indicates the stimulation electrode.

### 17. Neuromorphic photonic circuits to modulate neuronal excitability in epilepsy (Yasaman Heidari)

Epilepsy is a neurological disorder associated with the hyperexcitable neural network condition. Symptoms depend on the involved region of the brain. Therefore, they are different such as seizure, psychological and cognitive disorders. To modulate neuronal activity, conventional medicines are intermittently prescribed regardless of the accurate time of the emergence of the seizure. Therefore, there is no significant treatment for 30% of patients because of pharmacological resistance. To overcome these problems a hybrid electric/photonic chip is made to recognize and respond to the aberrant electrical activity of the neurons in a closed-loop way. The electric component of the system is involved in the learning process and in reading the neuronal activity via electrophysiology. The optical component is made of a photonic neural network and is used to recognize the seizure and, based on the electrical activity of the neurons, produces optical impulses to modulate optogenetically the abnormal neurons activity.

### 18. Nanostructures from nature: a sustainable perspective of innovative material production (Marina Scarpa, Paolo Bettotti, Elvira D'Amato, Guglielmo Trentini)

Some natural molecules are able to behave as building blocks of materials with remarkable properties and functions. These molecules are prone to form hierarchical structures, which bridge macroscale to molecular features, passing through fundamental structural elements whose dimension is within the nanoscale. In this regard, nanoscience and nanotechnology have to learn from nature to design structures, which have related analogs in biological materials, or to isolate nanostructures already present in nature and arrange them to obtain innovative and environmentally friendly materials. The nanoscale elements forming the cellulose structure (i.e. nanocrystals and nanofibers) are among the most promising natural materials, since they are easily obtained from vegetables and offer a wide spectrum of possible applications.

In recent years, we have developed procedures to isolate nanocrystals and nanofibers from the macroscopic cellulosic fibers by removing the amorphous domains. Cellulose nanocrystals are rigid sticks few hundreds nm long and with a cross section of about 10-20 nm<sup>2</sup>. Their surface chemistry is flexible and, upon proper surface functionalization, large amount of surface charge can be imparted onto specific crystalline planes. Thus, the electrostatic interactions between the charge bearing groups and the water environment in which they are dissolved permit to tune the material properties and to realize materials spanning either liquid, gel as well as solid state. These materials have proved to be effective to fabricate membranes with selective gas barrier properties or hydrogels (Fig. 29).

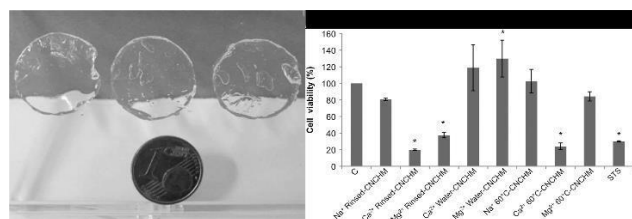


**Figure 29:** Nanocellulose gel patches; (right) Cell viability measured by washing the sample with different protocols. Untreated cells were used as control, first column.

Since 2019, we are exploring the possibility to recover high benefit products from renewable biomass sources, in particular from wastes of wood and food processing. Our aim is to obtain nanocellulose, silica and nutraceuticals using green chemistry approaches and use these molecules and nanostructures as building blocks of smart items such as bioplastics, non-flammable building materials, active hydrogel patches. Besides replacing the materials obtained from fossil fuels, the main expected advantage relies on the outstanding physical properties of the nano-sized components (namely fibrous and crystalline nanocellulose).

These properties have been extensively investigated in our Laboratory.

**For more info:**

Nanoscience Laboratory  
Department of Physics  
University of Trento  
via Sommarive 14  
38123 Povo - Trento (Italy)  
<http://nanolab.physics.unitn.it/>

Laboratory assistant  
Dr. Chiara Rindone  
email [chiara.rindone@unitn.it](mailto:chiara.rindone@unitn.it)  
phone +39 0461 283172